

## PAPER

View Article Online  
View Journal | View Issue



Cite this: *Environ. Sci.: Water Res. Technol.*, 2022, **8**, 1444

# Elucidating morphological effects in membrane mineral fouling using real-time particle imaging and impedance spectroscopy†

Chidiebere S. Nnebuo, , Denise Hambsch  and Oded Nir \*

Mineral fouling is a major hindrance to high recovery effluent nanofiltration, with calcium phosphate (Ca-P) and calcium carbonate (CaCO<sub>3</sub>) the most prevalent mineral foulants. In this study, we used a novel combination of real-time in-line microscopy, electrical impedance spectroscopy (EIS), post SEM analysis, and filtration metrics (water flux and rejection) to study mineral fouling mechanisms of Ca-P and CaCO<sub>3</sub> salts in synthetic effluent nanofiltration. We used nanofiltration (NF) polyelectrolyte multilayer (PEM) membranes, prepared by static layer-by-layer (LbL) coating of a cationic polymer – polydiallyl dimethylammonium chloride, and anionic polymer – poly styrenesulfonate (six bi-layer) on a polyethersulfone (PES) ultrafiltration (UF) membrane. Increasing permeate recovery over filtration time was simulated by adding CaCl<sub>2</sub> with NaHCO<sub>3</sub> or NaH<sub>2</sub>PO<sub>4</sub>/Na<sub>2</sub>HPO<sub>4</sub>. Using the novel combination of methods, we delineated the mechanisms governing fouling development with time for both CaCO<sub>3</sub> and Ca-P. For CaCO<sub>3</sub>, a transition from heterogeneous precipitation on the membrane surface (scaling) to particulate fouling due to bulk precipitation was identified. For Ca-P, a transition from fouling by amorphous particles to fouling by crystalline particles was identified; and this phase-change was captured in real-time images using an in-line microscope. We also found that for similar precipitation potentials measured by weight, Ca-P fouling was more detrimental to water flux (86% decrease) compared to CaCO<sub>3</sub> (20% decrease) due to the voluminous amorphous phase. We established in-line microscopy as a new useful method to study mineral fouling, as it gives invaluable information on the suspended particles in real-time. Combining it with EIS gives complementary information on mineral accumulation on the membrane surface. Insight from this study and further use of these methods can guide future strategies towards higher effluent recovery by membrane filtration.

Received 1st March 2022,  
Accepted 4th May 2022

DOI: 10.1039/d2ew00155a

rsc.li/es-water

## Water impact

We present the first use of in-line microscopy and real-time particle imaging as an effective technique for studying mineral fouling in membrane filtration. Complementary use of this technique with impedance spectroscopy delineates mechanisms governing mineral fouling and its morphological effects in wastewater effluent nanofiltration. This study provides insights on possibilities to control mineral fouling limiting sustainable high recovery effluent nanofiltration.

## 1. Introduction

Recycling of wastewater has a vital role in tackling global water scarcity, as the effluent is a largely untapped water resource with a stable supply year-round.<sup>1–5</sup> However, wastewater effluent contains various persistent contaminants that pose a risk to public health and the environment.<sup>6–9</sup> These contaminants may include excess phosphorus,

emerging/trace organic contaminants (ECs/TrOCs) such as pharmaceuticals and personal care products (PPCPs), endocrine disrupting compounds (EDCs), trace elements,<sup>9</sup> steroid hormones, surfactants, industrial chemicals,<sup>10</sup> pesticides and inorganic salts.<sup>6</sup> Since conventional wastewater treatment plants cannot properly remove these contaminants,<sup>10,11</sup> it is widely acknowledged today that further treatment is needed for sustainable reuse and safe discharge of tertiary effluent.

To attain various water quality requirements necessary for different wastewater recycling uses, membrane processes like reverse osmosis (RO) and nanofiltration (NF) have emerged as the best available technology.<sup>6,11–14</sup> RO membranes reject most dissolved molecules and thus can bring the tertiary

Department of Desalination and Water Treatment, Zuckerberg Institute for Water Research, Jacob Blaustein Institutes for Desert Research, Ben-Gurion University of the Negev, Sede-Boqer Campus, Midreshet Ben-Gurion, 84990, Israel. E-mail: [odni@bgu.ac.il](mailto:odni@bgu.ac.il)  
† Electronic supplementary information (ESI) available. See DOI: <https://doi.org/10.1039/d2ew00155a>

effluent to drinking-water quality level, enabling potable use, either directly (e.g., Singapore) or indirectly through aquifer recharge (e.g., California). NF membranes remove all microorganisms and most of the organic micropollutants and dissolved phosphorus (depending on membrane type). Therefore NF-treated effluent can be exploited for non-potable uses such as irrigation, rehabilitation of water supply to natural water bodies,<sup>1,7</sup> and creating artificial water bodies for recreational activities or ornamentation. While RO is the standard for potable reuse of tertiary effluent, using NF membranes offers some leverage over RO membranes in non-potable reuse; including lower operating pressure, tuneable selective removal of salts/solutes, and the availability of more robust membrane materials.<sup>13,15,16</sup> Therefore, in light of the global increase in wastewater reuse and stricter effluent discharge regulations, the application of RO and NF processes for wastewater treatment is expected to increase.

A key drawback to membrane processes application to wastewater recycling is the high cost of retentate stream management.<sup>17–20</sup> A retentate stream of RO/NF applied to wastewater, typically 10–30% of the feed water volume, contains the various contaminants removed from the effluent at higher concentrations. Therefore, there is a need to minimize the retentate volume by operating at a higher permeate recovery ratio to achieve cost-effective and sustainable RO/NF processes. However, the recovery ratio in effluent NF/RO is currently limited by chemical fouling, mainly caused by the precipitation of calcium phosphate (Ca-P) and calcium carbonate (CaCO<sub>3</sub>) minerals,<sup>21</sup> reaching supersaturation when concentrated in the retentate. Commonly used strategies for scaling control can be grouped into (a.) scalants removal by pre-treatment of feedwater (b.) scaling inhibitors use (c.) process-based strategies.<sup>22</sup> While, CaCO<sub>3</sub> scaling can be effectively controlled by adjusting the pH and use of antiscalants,<sup>23</sup> Ca-P minerals could precipitate at pH < 6, and no effective antiscalants are currently available for controlling Ca-P fouling.<sup>21,24–26</sup> Developing novel solutions calls for a better understanding of the chemical fouling mechanisms of these scalants during effluent filtration.

Mineral fouling occurs when sparingly soluble salts are rejected by the membrane, and consequently, their concentration increases in the retentate until it reaches a supersaturation level that is sufficiently high to induce precipitation.<sup>22</sup> Supersaturation is further increased near the membrane surface due to concentration polarization (CP).<sup>14,25,27,28</sup> The evolution and dynamics of mineral scaling are influenced by several factors including, pH,<sup>29</sup> flow velocity,<sup>28</sup> Ca/P ratio, presence of other salts (Mg<sup>2+</sup> for CaCO<sub>3</sub>),<sup>30,31</sup> operating pressure,<sup>28</sup> physicochemical membrane surface properties,<sup>32</sup> and ion rejection rate.<sup>33</sup> Mineral fouling can progress through homogeneous-like precipitation/crystallization in the bulk or heterogeneous surface crystallization.<sup>14,34,35</sup> Mineral particles formed in the bulk may deposit on the membrane surface to form a cake layer, whereas, in surface crystallization, the scaling layer

grows laterally on the membrane surface. Tzotzi *et al.* (2007)<sup>36</sup> identified heterogeneous-surface crystallization as the primary mechanism for CaCO<sub>3</sub> NF scaling of tap water, while Xu *et al.* (2010)<sup>37</sup> reported colloidal fouling as the primary mechanism of Ca-P salt in nanofiltration of effluent. While both routes can hinder filtration performances, removing a scaling layer is typically more challenging or even not practical.<sup>25</sup>

Although mineral fouling is affected by processes occurring both in the retentate and on the membrane surface, there are little or no reports on parallel measurements of these processes. Such data can, for instance, delineate between scaling and particulate fouling. Moreover, little or no attention was given to the role of mineral morphology in effluent nanofiltration. Elucidating morphological effects can be challenging, especially for Ca-P minerals, including multiple possible phases of different morphologies. We used a novel combination of in-line real-time particle microscopy and *in situ* electrochemical impedance spectroscopy (EIS) to address these knowledge gaps. We conducted nanofiltration experiments, where we gradually added scaling ions to simulate the increase in supersaturation and the accumulation of crystal mass associated with mineral fouling. The data collected from these novel systems, together with water and salt permeation data and post-filtration electron microscopy, elucidated the underlying micro-scale phenomena and the mechanistic differences between the two mineral types studied here. These differences affected the membrane performance and pointed toward different mitigation methods for Ca-P and CaCO<sub>3</sub> mineral fouling. Additionally, we used the extensively studied CaCO<sub>3</sub> mineral fouling to validate and distinguish its differences from Ca-P's mineral mechanisms and morphological effects as delineated by our novel technique.

## 2. Materials and method

### 2.1. Materials

The following chemicals were obtained from Merck company U.S.A.; MgSO<sub>4</sub>·7H<sub>2</sub>O; KCl; CaCl<sub>2</sub>·2H<sub>2</sub>O; NaCl; Na<sub>2</sub>HPO<sub>4</sub>·2H<sub>2</sub>O; NaH<sub>2</sub>PO<sub>4</sub>·H<sub>2</sub>O while NaHCO<sub>3</sub> and nitric acid (70%) were obtained from Bio-lab company Israel; AnalaR BDH Laboratory Supplies Israel supplied Na<sub>2</sub>HPO<sub>4</sub>; Sigma Aldrich supplied NaH<sub>2</sub>PO<sub>4</sub>. All chemicals were of analytical grade. Na<sub>2</sub>HPO<sub>4</sub> and NaH<sub>2</sub>PO<sub>4</sub> were used to make a phosphate buffer of 0.1 M (at a pH 7) in the ratio of 0.65:0.35. The phosphate (P) buffer was used throughout the experiments for membrane integrity P rejection tests. Polyethersulfone (PES) ultrafiltration (UF) membranes with molecular weight cut-off (MWCO) of 20 kDa were obtained from Sterlitech U.S. A; polydiallyldimethylammonium chloride (PDADMAC) MWCO = 400–500 kDa and poly(styrenesulfonate) (PSS) MWCO = 1000 kDa were also purchased from Sigma Aldrich while deionized (DI) water <2 μS cm<sup>−1</sup> was used during the experiments. The procedure for layer-by-layer coating of PES membrane into an NF polyelectrolyte multilayer membrane

(PEMM) is available in the ESI† S1.0. NF-PEMM were used in this study for its competitive advantages over commercial NF membranes like: backwash potential; tuneable monovalent/divalent ions selectivity; mechanochemical stability at extreme pH ranges (acid cleaning); and regeneration-ability.<sup>38–40</sup> Due to its selectivity, divalent cations ( $\text{Mg}^{2+}$ ,  $\text{Ca}^{2+}$ ) and some monovalent ions ( $\text{Na}^+$ ,  $\text{K}^+$ ,  $\text{Cl}^-$ ) are partially permeated, thus contributing to both fouling control and broad range permeate reuse (agriculture, drinking, *etc.*) in a high water recovery wastewater effluent filtration. Unlike commercial membranes where precipitation must be avoided, for NF-PEMM membranes, some precipitation can be allowed during filtration due to their high stability during different cleaning procedures.

## 2.2. V19 particle view microscope

V19 Particle view™ Mettler Toledo AG (U.S.A) is a probe-based video microscope and an in-line *in situ* tool for

real-time monitoring of the particle development in the feed during filtration. Particle V19 (iC PVM) measurement is a particle vision measurement (PVM) technology – a non-invasive tool that can capture and visualize particle development in real-time. iC PVM emits a laser that illuminates the particles within the microscope probe window, and particles reflect the laser into the probe. The probe captures the reflected image through its camera. Each captured image has a known brightness and intensity, with the ratios of the former and later giving the reflectivity of the system as relative backscatter index (RBI). iC PVM software calculates the RBI, and its analysis with captured images gives the changes in the particles' shape, size, and concentration. Functional specifications of Particle view V19 are  $1300\ \mu\text{m} \times 890\ \mu\text{m}$  ( $\pm 50\ \mu\text{m}$ ) field of view,  $>2\ \mu\text{m}$  optical resolution,  $1500 \times 1024$  pixels image resolution, and eight pulsed laser diodes (4 front; 4 back) illumination (Fig. S8†). Settings used during the experiment are: front light with auto adjust, the focus was

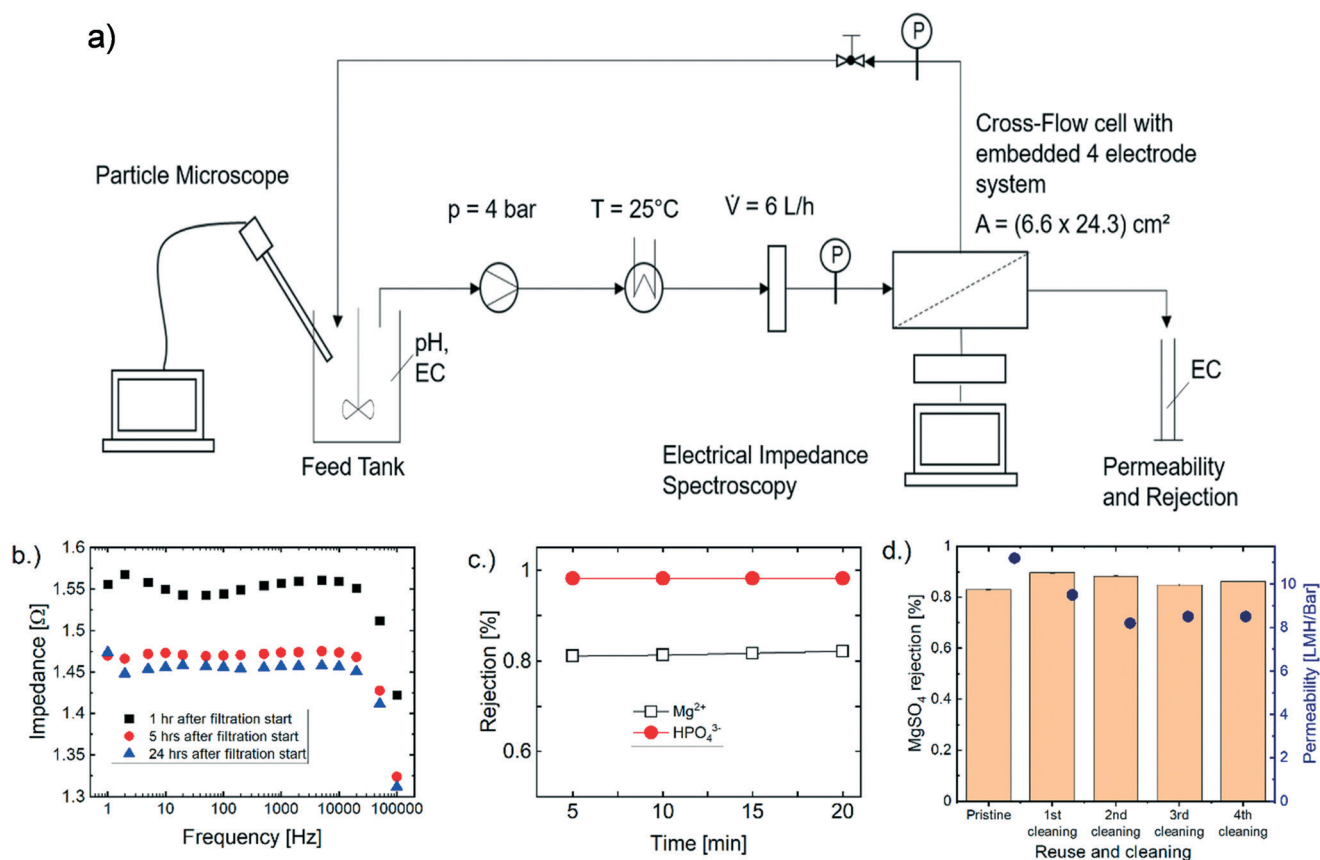


**Fig. 1** (a) Schematic of the nanofiltration experimental set-up with in-line particle microscope and *in situ* electrical impedance spectroscopy, enabling real-time monitoring of mineral fouling. (b) Typical EIS scan of the entire frequency range (1– $10^5$  Hz), which was similar for all experiments. Data shown for  $\text{CaCO}_3$  mineral scaling under low supersaturation. Weak dependence on frequency was demonstrated, with lower frequencies (1–10 Hz) generally being the most stable. Frequency  $\omega = 5$  Hz was selected for probing the fouling layer resistance. (c) Rejections of magnesium and hydrogen phosphate at 5 bars in a rejection experiment for the same membrane and the same setup (except particle microscope and EIS) and (d) magnesium sulphate rejections and water permeability for the NF-PEMM membrane before and after 4 cycles of filtration and cleaning. Rejections were tested at the same pump frequency (100 Hz) and several pressures; 3 bar, 4 bar, 5 bar, 6 bar, and 7 bar for 0.05 M of hydrogen phosphate while 1 bar, 3 bar, and 5 bar for 0.02 M of magnesium, respectively. All rejections results were similar for all pressures tested; hence, only rejection results of 5 bar are presented here.

moved 100  $\mu\text{m}$  away, with sharpening and enhance features selected.

### 2.3. Filtration experiments

All experiments were performed in full recirculation mode, with permeate and retentate recycled into the feed tank. Concentrated synthetic wastewater effluent according to Shafdan composition<sup>41</sup> (Table S3†) was used. Experiments were performed in three stages: (i.) compaction filtration using DI for 18 hours to achieve stable flux and minimize sample and reference noise of the impedance spectra; (ii.) conditioning filtration – DI water was replaced with feed solution (concentrated synthetic effluent) without the scaling salt components, and filtration runs for 2 hours; and (iii.) filtration experiments – started with the addition of the scaling salts (Table S4†) accordingly. PHREEQC was used to model similar mass-based precipitation potential for both scalants in each experiment to determine the concentration of added scaling salt components. Details about PHREEQC are available at S2.0.† Experimental set-up (Fig. 1a) had a 2 L feed tank stirred with a mechanical stirrer set at 200 rpm throughout the experiments. The feed tank was connected *via* a gear pump (FluidOTech) to the INPHAZE™ filtration module, which contained the membrane. The pump was coupled with a frequency converter (EDS1000 Inverter, ENC), enabling the adjustment of the feed flow rate. Before entering the filtration module, the solution passed through a customized chiller (MRC), keeping the temperature at  $25 \pm 1$  °C. Two gauges at the inlet and outlet of the module measure the transmembrane pressure (TMP). TMP at the flowcell's outlet could be regulated by a back-pressure valve (Swagelok) from 0 to 7 bars. Additionally, the retentate flow was monitored by a rotameter type flowmeter (ASV Stubbe).

The membrane sample size for the crossflow-chamber of the INPHAZE™ filtration module was 243 mm  $\times$  66 mm, giving an effective membrane area of 0.016 m<sup>2</sup>. The INPHAZE™ is a high-resolution EIS with impedance range: 0.1–10<sup>11</sup>  $\Omega$ , frequency range: 10<sup>−3</sup>–10<sup>6</sup> Hz, phase resolution: 0.001°, and magnitude resolution: 0.002%. The INPHAZE™ filtration module is connected with a four electrodes system which is connected to the spectrometer unit and in turn connected to a computer. Detailed description of the EIS crossflow cell can be found at S5.0.† Our focus in using EIS was to investigate dynamic scaling processes occurring over relatively short timescales. Therefore, impedance measurements analysis was based on a single frequency, 5 Hz (Fig. 1b), in which the dependency of impedance on frequency was weak (phase was almost zero). Therefore, at this frequency, the EIS value can be considered as pure electric resistance. The same approach was applied for membrane fouling in previous studies.<sup>42,43</sup> The pressure for all experiments was constant at  $p = 4$  bars with a feed flow rate of  $\dot{V} = 6$  L h<sup>−1</sup>. The experiments were modified according

to Fig. S3 and S4† to study different aspects of scaling. A summary of differences in the experiments can be found in Table S5.† Fig. S5† shows the experimental cycle used for all experiments.

## 3. Results and discussion

Following compaction and pre-conditioning stages, the filtration stage commenced with additions of 7 aliquots of CaCO<sub>3</sub> (CaCl<sub>2</sub>/NaHCO<sub>3</sub>; 8 mM each) or Ca-P (CaCl<sub>2</sub>/Na<sub>2</sub>HPO<sub>4</sub>; 6 and 4 mM each from 1 M stock solutions) salts respectively at 20 minutes intervals to the feed tank during 4 h filtration run for the high supersaturation experiments. These main experiments were repeated with reproducible results (Fig. S15 and S16†). Modifications to the main experiments were made to the experimental procedure to investigate the different stages of fouling. Permeate flux, observed salt rejection, electrical conductivity (EC), electrical impedance spectroscopy, and *in situ* online imaging (RBI and images) of crystal evolution in the feed tank were recorded in real-time during all the filtration experiments.

### 3.1. CaCO<sub>3</sub> mineral fouling at high supersaturation

Three distinct stages in the evolution of normalized flux and electrical resistance (Fig. 2a) appeared during the filtration of synthetic effluent supersaturated with CaCO<sub>3</sub>. This observation is consistent with data obtained in repeat experiments (Fig. S15†), indicating the reproducibility of the experiments. In the first stage ( $t \sim 0$ –1.2 h), the flux decreases sharply by 25%, while at the same time, the electrical resistance of the fouling layer increased from  $\sim 0$  to 1.95  $\Omega$ . In the second stage ( $t \sim 1.2$ –1.9 h), the flux increased by 8.0%, while the electrical resistance of the fouling layer increased moderately, reaching a peak of 2.02  $\Omega$ . In the third and final stage ( $t \sim 1.9$ –4 h), the flux decreased moderately by 6.0% until  $t = 3.35$  h and remained unchanged until the end of the experiment (4 h). During that time, the electrical resistance of the fouling layer decreased slightly, reaching  $\sim 1.9$   $\Omega$ —this complex behaviour of flux and electrical resistance hints that different fouling mechanisms were in action during filtration. Using real-time imaging (Fig. 2d) and light scattering (RBI) (Fig. 2b) of mineral particles in the recycled feed solution in combination with the real-time electrical resistance and flux measurements can underpin the dominant fouling mechanisms at each stage.

Our results indicate that the first stage of fouling was dominated by CaCO<sub>3</sub> scaling, *i.e.*, the increase in fouling layer resistance is typical to scaling<sup>44</sup>—the formation of a rigid crystalline layer that completely blocks water and ion transport through the impacted membrane surface fragment. Accordingly, the RBI (Fig. 2b) remained constant in the first 0.5 hours, and no particles were observed in the feed tank by the in-line microscope (Fig. 2d-T<sub>2</sub>). The sharp increase in RBI after 0.5 h is likely due to the formation of sub-micron crystal clusters (too small to be captured in images), marking the beginning of homogeneous precipitation. These tiny particles



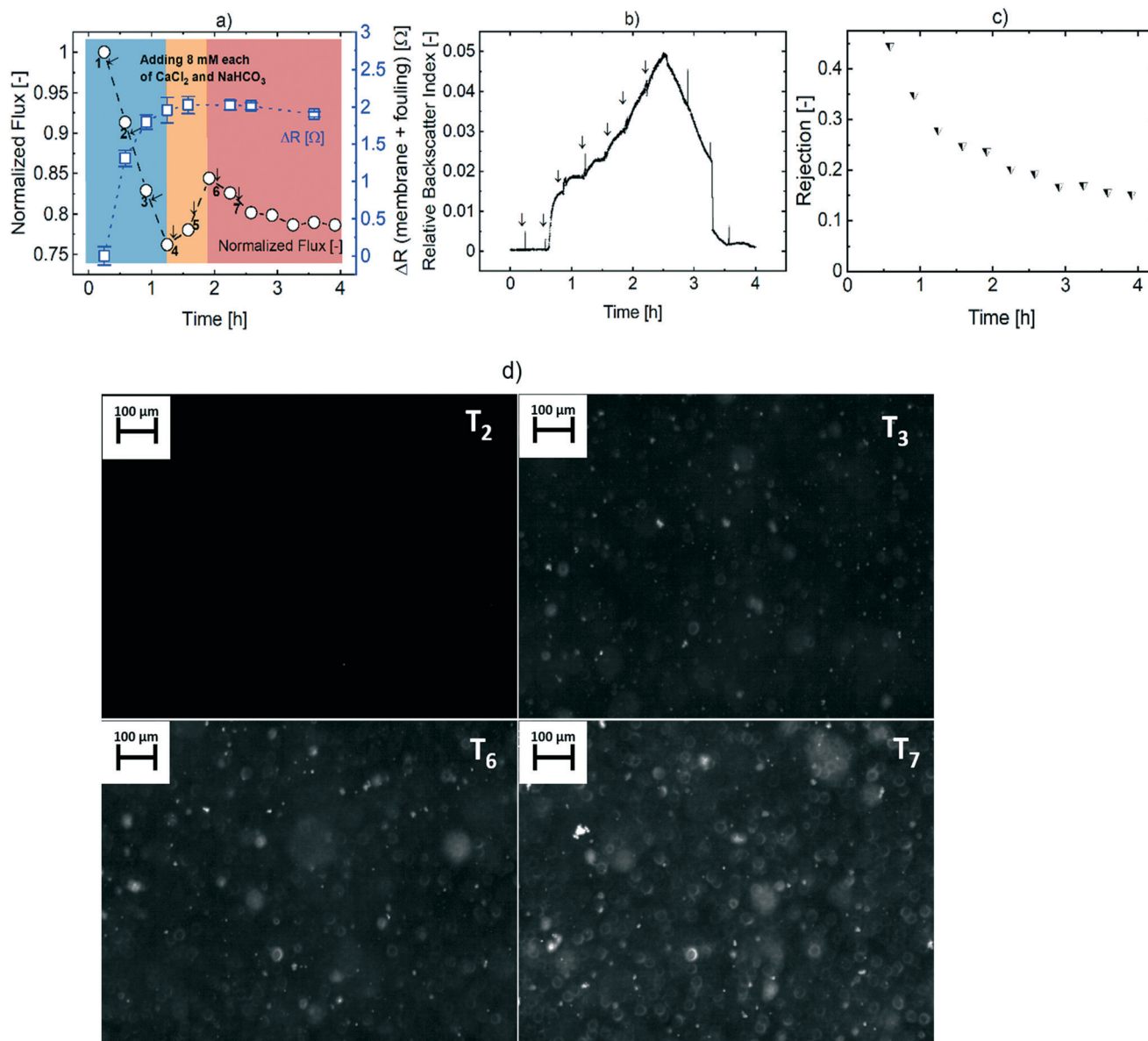


**Fig. 2** Data recorded during nanofiltration of solutions highly supersaturated with calcium carbonate (a) normalized flux-(○) (arrows everywhere in all figures indicate the addition of scaling components, immediately after permeability measurement. The first point is the permeability of background solution without scaling salts, all permeability normalized to initial permeability while T<sub>1-2</sub> (T<sub>1</sub> figure is identical to T<sub>2</sub> and is not shown) indicate blank before 1st and 2nd scaling salts was added with precipitation occurring after 2nd addition) and membrane resistance-(□) [Ω] (b) RBI [-] evolution, (c) salt rejection - (▽), (d) and in-line real-time microscope images at 4 time points (T<sub>2</sub>-T<sub>3</sub>-T<sub>6</sub>-T<sub>7</sub>) for concentrated effluents NF with CaCO<sub>3</sub>. Electrical resistance data points are an average of multiple measurements ( $N = 6-10$ ), where error bars are standard deviations. Similar trends are observed in two replicate experiments (Fig. S15†), indicating the experiments' reproducibility.

were bound to accumulate on the membrane surface and increasingly contribute to both electrical and hydraulic resistances together with the scaling layer, which was likely still the dominant mechanism at  $t \sim 0-1.2$  h.

At the second stage,  $t \sim 1.2-2$  h, the results indicated a gradual transition from mineral scaling to particulate fouling. The transition was driven by the increase of CaCO<sub>3</sub> crystals size, as apparent from the PVM images (Fig. 2d at T<sub>3</sub> and T<sub>6</sub>). The progress of the bulk crystallization process is also indicated by the linear increase in RBI at  $\sim 1.2-2$  h. A surprising increase in permeate flux was observed at this

stage in two out of three repetitions, while at the third repetition, a plateau in flux was recorded (Fig. S15b†). We attribute this trend reversal (or plateau) to further growth of the previously ( $t \sim 0.6-1$  h) deposited sub-micron crystals, since larger particles are more affected by shear-induced diffusion.<sup>45</sup> It should be noted that this phenomenon is highly dependent on random coverage pattern in the scaling onset and thus occurs at different times and magnitudes. Nevertheless, the flux trend change indicates a transition to a different fouling mechanism. The flattening of the fouling layer electric resistance curve (Fig. 2a and in S15†) further

supports the transition to the deposition of a cake layer comprising larger particles and consequently larger average pore size with higher ion conductance.

In the third stage,  $t \sim 2\text{--}4$  h, our results suggest a complete shift to a particulate fouling regime. This was expressed in a milder decrease in flux with time relative to the 1st stage and a small yet distinct reduction in the electrical resistance. The latter can be attributed to cake-enhanced concentration polarisation (CECP), which was previously shown to increase the conductance of the fouling layer.<sup>44</sup> The steady increase in RBI at  $t \sim 2\text{--}2.5$  h (Fig. 2b) and the PVM images taken at  $t \sim 2\text{--}2.15$  h (Fig. 2d, T<sub>6</sub> and T<sub>7</sub>) point to further growth of CaCO<sub>3</sub> crystals in the bulk, which resulted in the formation of a cake layer. At  $t \sim 2.5\text{--}4$  h, the RBI (Fig. 2b) decreased per a decrease in the particle concentration in the feed seen in the PVM image recorded at  $t = 3.25$  h (Fig. S20†). This is due to the build-up of particles on the membrane surface, as the further decrease in flux suggests. The radically different consequences to filtration performance associated with the different fouling regimes have prompted us to conduct additional experiments to differentiate between scaling and particulate fouling as described below.

### 3.2. CaCO<sub>3</sub> mineral fouling under low supersaturation

To reinforce our findings on the signals caused by CaCO<sub>3</sub> mineral scaling, we simulated low supersaturation in the feed

to suppress bulk crystallization. This was done by extending the intervals between scaling salt additions to 1 h or more. At  $t \sim 0\text{--}0.5$  h, the normalized flux and electrical resistance (Fig. 3a) trends were similar to the previous experiment, as the flux decreased sharply by 9.0% and the electrical resistance of the fouling layer increased. At the same time, the RBI (Fig. 3b) remained unchanged for  $t < 0.5$  h, confirming that no particles were present in the bulk – an indication of heterogeneous mineral scaling. At  $t > 0.5$  h, the RBI increased due to the emergence of nanoparticles, too small to be captured as images by the in-line microscope. In the high supersaturation experiment, a second aliquot of scalants was added at this point, resulting in the continuation of the flux decline in the same trend. This time, however, the flux decline was flattened with the increase in RBI, which can be attributed either to fouling by nanoparticles or to a slower scaling formation due to competition with the nanoparticles' surface and lower bulk supersaturation. Accordingly, the increase in electrical resistance was flattened again, further demonstrating the high sensitivity of this method to the type of mineral fouling. At  $t = 1$  h, a second dose of scalants was added, initiating a complete transition to particulate fouling. This was indicated by the in-line imaging (S11-T<sub>2-3</sub>†), the sharp increase in RBI, the flattening in flux decline, and the moderate decrease in fouling layer electrical resistance, as in the previous set of experiments. This time, however, post-filtration SEM imaging provided additional information.

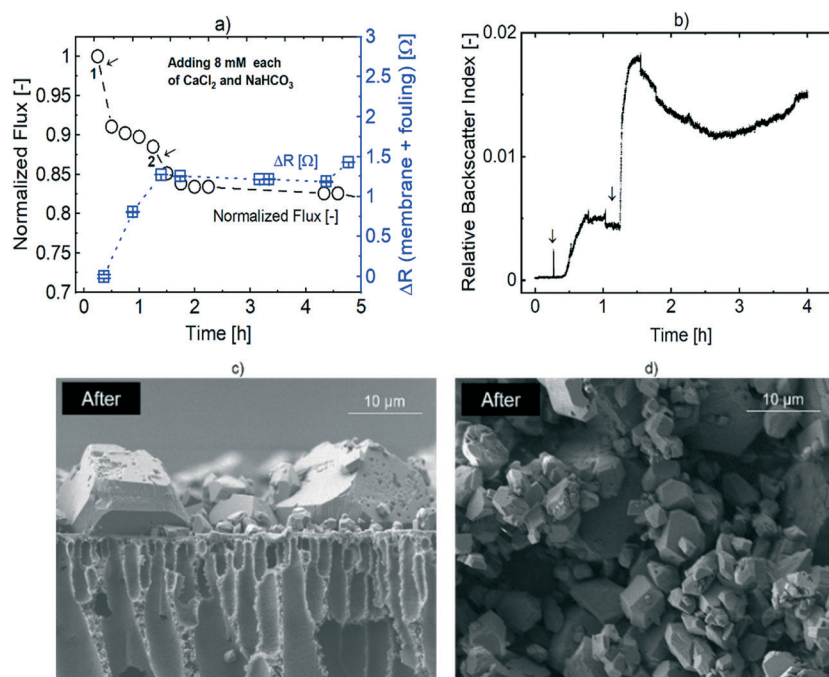


**Fig. 3** Data recorded during and after filtration for the low supersaturation CaCO<sub>3</sub> scaling experiment; (a) permeability-(○) and membrane resistance-(□) [Ω] (b) RBI [-] evolution; SEM images taken after filtration; (c) cross-section; (d) top view, with 2500× magnifications. Electrical resistance data points are an average of multiple measurements ( $N = 10$ ), where error bars are standard deviations. SEM images show crystalline particles of various sizes; large particles ( $>15 \mu\text{m}$ ) heterogeneously grew laterally on the membrane surface due to surface crystallization/scaling before homogenous crystallization. Smaller particles ( $<5 \mu\text{m}$ ) are due to homogenous crystallization. The extended graph until 24 h time can be found in Fig. S18†

SEM images of the  $\text{CaCO}_3$  crystals deposited on the membrane surface (Fig. 3c) further reinforced our hypothesis regarding the dominant fouling mechanism. The deposited particles had crystalline rhombohedral sharp and straight edges – typical of calcite polymorphs,<sup>46</sup> the most stable form of  $\text{CaCO}_3$ . The large particles ( $>15\ \mu\text{m}$ ) appearing in the cross-sectional image (Fig. 3c) and overshadowed in the bulk suspension imaging by smaller particles ( $\text{S11-T}_{2-3}\dagger$ ) suggest lateral growth on the membrane surface, affirming the assumption of heterogeneous crystallization. According to the SEM images, scaling was developed as separate ‘islands’ that grew on the membrane and blocked the transfer of water and ions. The smaller ( $<5\ \mu\text{m}$ ) particles seen in between (Fig. 3c) and on top of (Fig. 3d) the larger particles corroborate our finding that particulate fouling took place after mineral scaling. The results of the particulate fouling experiment described below confirm that the smaller particles originated from bulk crystallization.

### 3.3. Particulate fouling by $\text{CaCO}_3$ crystals

To reinforce our interpretations regarding the signals caused by particulate fouling of  $\text{CaCO}_3$  precipitates, we induced

homogenous bulk crystallization in the feed tank before initiating filtration. This was done by adding 7 aliquots of 8 mM ( $\text{CaCl}_2/\text{NaHCO}_3$ ) in intervals of 20 minutes, as in the high supersaturation experiments. The crystals' growth was evident from the monotonic increase in RBI (Fig. 4b) at  $t \sim 2.2\text{--}2.9\ \text{h}$ . The sharp increase in RBI after filtration started may be due to the change in flow around the probe in the feed tank. As seen in Fig. 4a, the normalized flux increased by 4–6%, while the electrical resistance of the membrane and fouling layer decreased by  $\sim 0.8\ \Omega$ . These signals are an amplified response to particulate fouling (as observed in the final fouling stage, section 3.1), *i.e.*, negligible addition to the hydraulic resistance and cake enhanced concentration polarization. The latter is also supported by the decrease in observed salt rejection (Fig. 4c) and is similar to the observed rejection in the final fouling stage (Fig. 2c) of the high supersaturation experiment. The SEM images (Fig. 4d and e) taken after filtration show a relatively homogeneous size distribution of the crystals, typical of bulk crystallization. The large crystals, indicative of their lateral growth on the membrane surface (as observed in Fig. 3c and d) are not seen in this case. The porous structure of the fouling layer, which

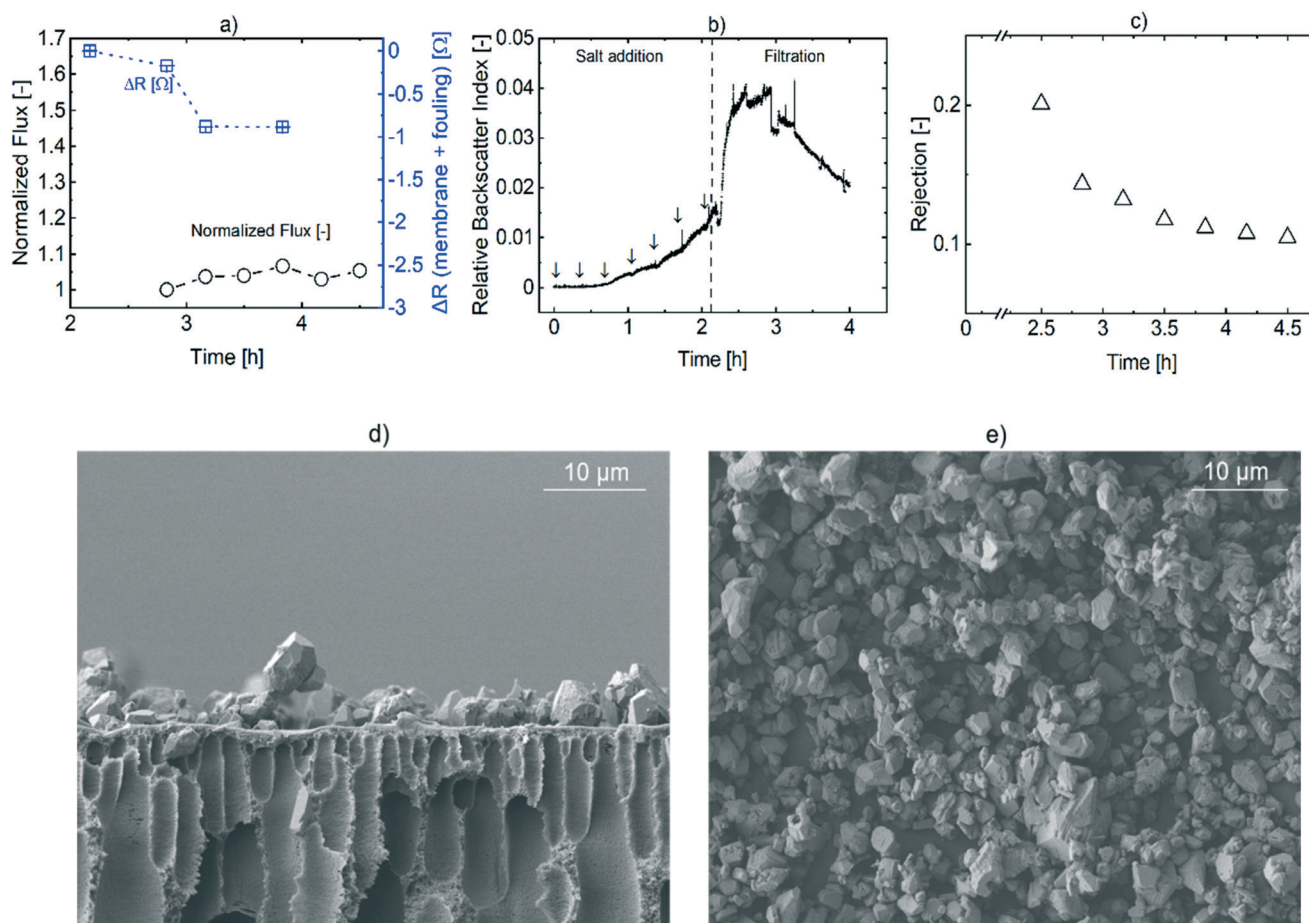


**Fig. 4** Data recorded during nanofiltration of calcium carbonate particles suspension in the bulk crystallization - cake filtration experiments; (a) permeability-(○) and membrane resistance-(□) [Ω] (b) RBI [-] evolution; (c) salt rejection - (Δ); SEM images (cross-section (d), and top view (e) with 2500× magnifications). Electrical resistance data points are an average of multiple measurements ( $N = 4\text{--}10$ ), where error bars are standard deviations.



causes the effects described above, is clearly seen. This further affirms our interpretation of the EIS and flux signals.

### 3.4. Rapid increase of calcium phosphate supersaturation

The trend of normalized flux vs. time (Fig. 5a) during filtration of synthetic effluent supersaturated with Ca-P was similar to that observed for  $\text{CaCO}_3$ . Similarly, this trend is consistent with data obtained from repeat experiments (Fig. S16†), indicating the reproducibility of our experiments. The trend in electrical resistance of the fouling layer was also similar; however, the time synchronization of this signal with the flux signal differs in the case of Ca-P fouling. As in  $\text{CaCO}_3$  fouling, three distinct stages of flux evolution were recorded:

a first stage ( $t \sim 0\text{--}1$  h) in which the flux decreased sharply (43%), a second stage in which the flux increased ( $t \sim 1\text{--}1.25$  h), and a third stage in which the flux decreased gradually (by  $\sim 14\%$ ). At the same time, the fouling layer electrical resistance was negligible in the first 0.5 h (according to the absolute value shown in the Fig. S21†), increased from  $\sim 0$  to  $\sim 1\ \Omega$  at  $t \sim 0.5\text{--}1.25$  h, then increased gradually until 2.5 h, before reaching a plateau at  $\sim 1.3\ \Omega$ . Although the trends in flux and EIS are similar between  $\text{CaCO}_3$  and Ca-P, the signals are synchronized differently in time, pointing at a different fouling mechanism.

By combining flux and EIS (Fig. 5a) with real-time microscopy (Fig. 5b and d), we were able to pinpoint the mechanisms underlying membrane fouling by Ca-P minerals,

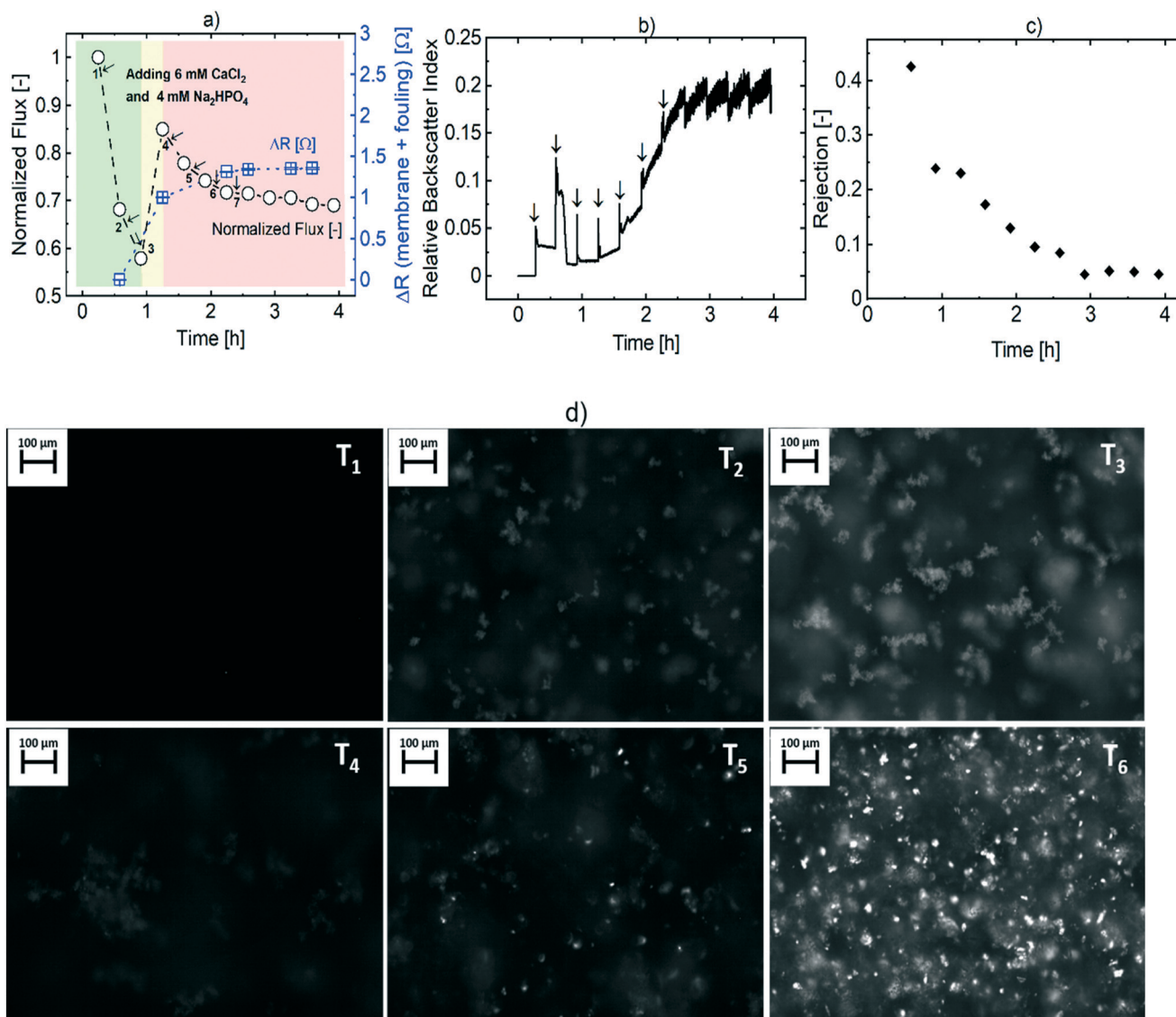


**Fig. 5** Data recorded during nanofiltration of solutions highly supersaturated with calcium phosphate (a) permeability-(○) and membrane resistance-(□) [ $\Omega$ ]; (b) RBI [-] evolution; (c) salt rejection - (◆); (d) in-line real-time microscope images at different time stages of filtration (T<sub>1</sub>–T<sub>6</sub>). T<sub>1</sub> indicate blank before 1st scaling salt was added and consequent precipitation followed. Electrical resistance data points are an average of multiple measurements ( $N = 10$ ), with standard deviations error bars. Similar trends are observed in the two replicate experiments (Fig. S16†) indicating the reproducibility of the experiments.



as it evolved during the nanofiltration experiment. Immediately after the first salt addition, the RBI (Fig. 5b) increased, implying that bulk precipitation already occurred at this early stage. This conclusion was supported by an independent experiment (Fig. S10<sup>†</sup>), in which we found that Ca-P precipitation starts at close to zero (0.0) supersaturation of ACP and with a very short induction time ( $\sim 50$ – $100$  seconds). The sharp flux decrease in this initial stage is thus attributed to the accumulation of sub-micron, highly hydrated, amorphous particles, which created a fouling layer of high hydraulic resistance. Ions, in contrast, could easily pass through this layer, indicating its porosity. After 0.5 h (before the 2nd salt addition), the real-time imaging (Fig. 5d-T<sub>2</sub>) reveals aggregates of particles with distinct ‘fluffy’ morphology and low light reflectance, thus affirming bulk precipitation of amorphous particles. After the 2nd salt addition, the number of particles and size of the aggregates in the bulk further increase (Fig. 5d-T<sub>3</sub>), leading to an additional decrease in flux. Following the 3rd salt addition,

the normalized flux increased from its minimum at 0.57 back to 0.85, while the electrical resistance increased sharply, indicating a change in the morphology of the layer. Indeed, the real-time particle imaging revealed a transition from amorphous precipitants (Fig. 5d, T<sub>1–3</sub>), first to a less ‘flaky’ and more interconnected aggregates (Fig. 5d T<sub>4</sub>), and then to a mixed-phase with crystalline components having a defined shape and high reflectance (Fig. 5d T<sub>5–6</sub>). It should be noted that the circulating feed solution is in direct contact with both the suspended particles, which were captured by the real-time imaging system and the particles in the fouling layer. Therefore, particle growth and phase transition observed in the bulk are also expected in the fouling layer, where these processes can be accelerated by concentration polarization. After this transition, the RBI increased and particle imaging indicated crystal growth in the bulk, corresponding to typical cake filtration, *i.e.*, slow reduction in flux and negligible change in electrical resistance.

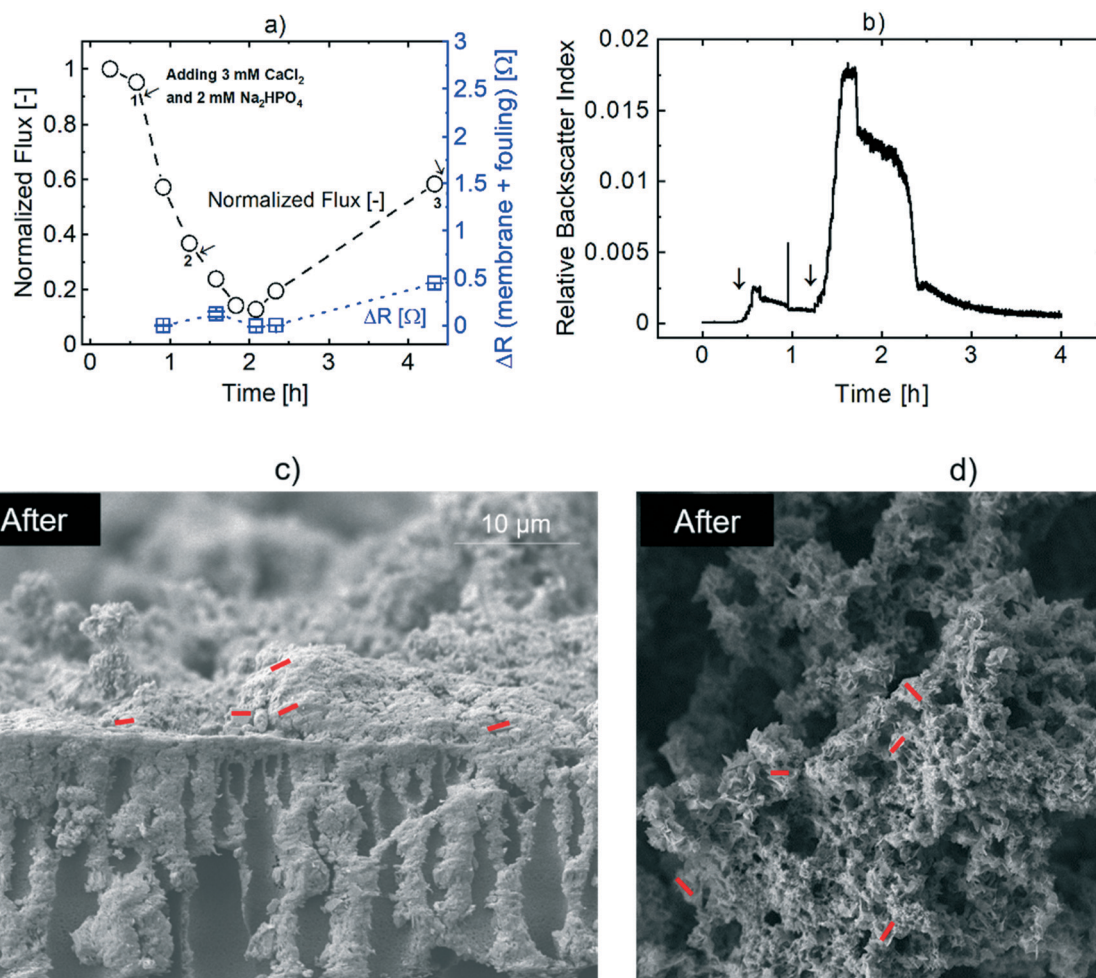


**Fig. 6** Data recorded during and after nanofiltration of solutions having low supersaturation with calcium phosphate (a) permeability-(○) and membrane resistance-(□) [Ω] (b) RBI [-] evolution; SEM images: (cross-sections; (c), and top view (d) after filtration with 2500× magnifications). Small red stripes indicate flat crystalline surfaces. Bulk crystallization is dominant and subsequent particles deposition – forming an impermeable cake layer. The extended graph until 24 h time can be found in Fig. S19<sup>†</sup>. Electrical resistance data points are an average of multiple measurements ( $N = 10$ ), where error bars are standard deviations.

### 3.5. Slow increase of calcium phosphate supersaturation

To further understand the initial, rapid increase supersaturation fouling stage of Ca-P fouling and to test our interpretation regarding the mechanism, we conducted another fouling experiment, where we increased the duration of low supersaturation. This was done by (1) adding half the amount of salt in every aliquot; (2) extending the intervals between salt aliquot addition to avoid fast crystallization, and; (3) splitting each aliquot into 10 equal small doses (2 min interval) to avoid high local concentration. This procedure resulted in fouling effects similar to those described in the initial stages of the previous section, yet more 'stretched' in time, allowing us to explore this stage with better time resolution.

The results reinforce our understanding of Ca-P fouling under slow supersaturation increase and align with the results obtained for the rapid supersaturation increase (section 3.4). After the 1st salt addition, the RBI (Fig. 6b) increased after a very short induction time, as before, then gradually decreased due to aggregation, and increased yet again after the 2nd salt addition. The RBI evolution supports the premise of Ca-P bulk precipitation as a primary fouling initiator. Due to the prolonged dominance of small particles in the circulating feed, the flux dramatically decreased by 64% and 86% after the 1st and 2nd additions, respectively, despite the lower amount of scalants added compared to the rapid supersaturation increase. This demonstrates the significant role of fouling layer morphology, influenced by the rate at which supersaturation increases. At the same time, the low and relatively constant electrical resistance value during the 1st 2.5 h supports the premise of a porous layer with good ion conduction and poor water conduction properties.

The results obtained at longer times (>2.5 h), during the slow increase of Ca-P supersaturation, further support our interpretation of the results obtained during the rapid supersaturation increase (section 3.4). Both the flux and EIS increased, showing the same trend as in section 3.4, yet after a longer time, due to lower concentrations of Ca and P. With this improved time resolution, it is visible that both the flux and EIS signals increased at the same time (Fig. 6a), reinforcing the premise of a morphological change in the fouling layer. It is generally known that amorphous particles (ACP) is a precursor phase for Ca-P precipitation and transforms to crystalline polymorphs – a process described by Oswald's rule.<sup>47,48</sup> We thus pose that dehydration and crystallization processes have condensed the layer, causing deswelling, which opened channels for faster water transport but reduced the surface available for ion transport. Condensation and dehydration of aggregates were previously recorded during the ageing of amorphous Ca-P.<sup>49</sup> Evidence for a phase transition can also be seen in the SEM images taken post-filtration. In both cross-sectional (Fig. 6c) and top view (Fig. 6d), flat surfaces (indicated by small red strips) of higher crystallinity can be spotted within the dense semi-

porous fouling layer. Precipitant seen below the membrane surface is probably minerals that were smeared on the cross-section when cutting the membrane in preparation for SEM imaging. Intra-pore fouling is not likely because the rejection of hydrogen phosphate by this membrane is very high (>90% see independent experiment in Fig. 1c). In this stage, the drop in RBI indicates the aggregation of small particles, which is a precursor for Ca-P phase transformation and crystal growth.<sup>49,50</sup>

### 3.6. Particulate fouling by Ca-P crystals

To isolate the effect of fouling by the more crystalline Ca-P phase, we induced bulk precipitation in the feed tank by adding 7 aliquots of scaling salts ( $\text{CaCl}_2/\text{Na}_2\text{HPO}_4$ , 6 and 4 mM, respectively), at 20 minutes interval prior to the filtration step. After the first two additions, the RBI signal (Fig. 7b) sharply increased due to the rapid formation of small particles. After the third addition, the RBI decreased due to aggregation followed by crystallization, as was also captured by the in-line imaging system (Fig. S14-T<sub>3</sub>†). The RBI remained low until filtration started (apart from local spikes on salt additions), indicating that no secondary nucleation has occurred. The RBI increased with the beginning of filtration (and the end of salt additions), likely due to shear forces causing the aggregates to break. As expected in fouling by large particles, the flux and electrical resistance (Fig. 7a) (9% and  $\Delta R = -0.25 \Omega$  respectively) slightly decreased. The decrease in salt rejection (Fig. 7c) further supported the occurrence of CECP. Overall, the trends in RBI, flux, and electrical resistance recorded during this induced fouling by Ca-P matches our interpretation of the final stage during the rapid increase of Ca-P supersaturation (section 3.4).

The SEM images (Fig. 7d and e) reveal the morphology of the Ca-P precipitants and the fouling layer they have formed on the membrane surface. A mixed layer is seen, containing amorphous-looking aggregates, together with crystal platelets. The cross-sectional image (Fig. 7d) reveals significant variations in the layer thickness that can be attributed to its heterogeneity. This heterogeneity is visible in the top-view image (Fig. 7e), also showing the contrast between the two phases. Compared to the fouling layer seen after the slow increase in Ca-P supersaturation (Fig. 6c), the amorphous phase is similar but seems less dense and more porous. It also appears that the deposited crystals disturbed the formation of a continuous dense layer, which again highlights the importance of morphology in mineral fouling.

## 4. Summary and conclusions

In this work, we studied membrane fouling by  $\text{CaCO}_3$  and Ca-P minerals, using a novel combination of real-time probing techniques: in-line particle imaging and EIS. This combination was found highly useful, enabling us to uncover scaling mechanisms and distinguish between them. Using these methods to study fouling by other minerals, such as



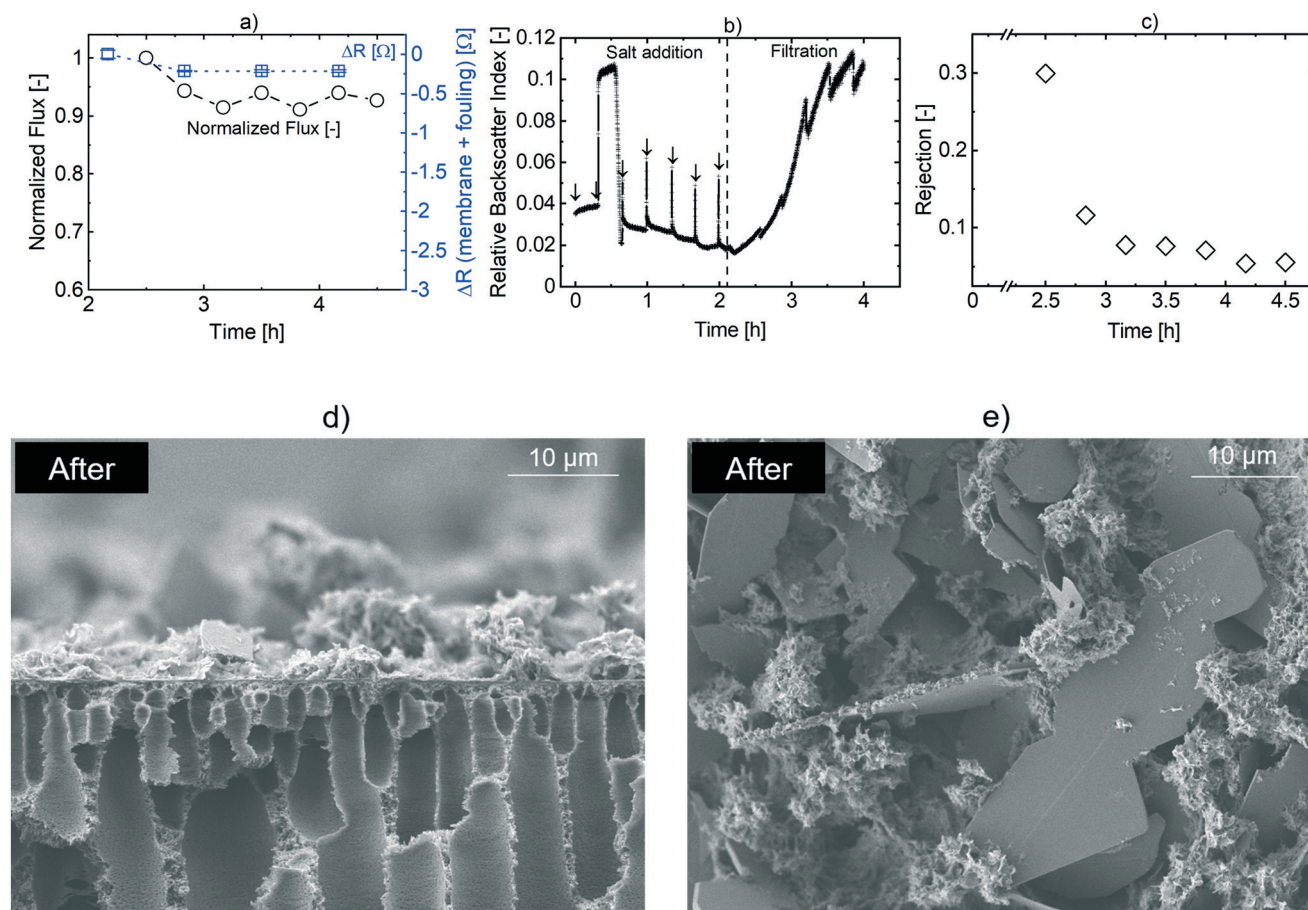


**Fig. 7** Data recorded during nanofiltration of calcium phosphate particle suspension in the bulk crystallization-cake filtration experiments (a) permeability-(○) and membrane resistance-(□) [Ω]; (b) RBI [-] evolution; (c) salt rejection-(◇); SEM images: (cross-section (d), top view (e), with 2500× magnifications). Electrical resistance data points are an average of multiple measurements ( $N = 10$ ), where error bars are standard deviations.

silica or iron oxides, will likely result in further insights. Complementary data gathered from iC PVM, EIS, flux measurement, and post-filtration SEM imaging was used to reconstruct how morphological changes induced by, *e.g.*, aggregation, particle growth, and crystallization determine the development of mineral fouling and its impact on filtration. The morphological changes were found to depend on the mineral type, filtration time, and rate of supersaturation increase.

For  $\text{CaCO}_3$  (Fig. 8a), the results imply that upon the increase in supersaturation, heterogeneous precipitation on the membrane surface began, forming impermeable scaling 'islands' on the membrane surface. Consequently, the surface available for the transport of both water and ions decreased. Upon further increase in supersaturation, the crystalline scaling islands grew towards the sides and the top, further reducing flux and ion conductance. At the same time, sub-micron particles started to form *via* bulk precipitation. Deposition of these small particles between the scaling islands decreased the water flux but had a negligible effect on ion passage. With further supersaturation increase and longer filtration time, the surface area of the suspended

particles gradually increased (with their size and number) until it overshadowed the surface area of the scaling islands. This marked a transition from a scaling regime to a particulate fouling regime. At the same time, the particles in the fouling layer also grew (some possibly sheared of the membrane surface), thus enabling faster water transport and partial recovery of the water flux. With further increase in supersaturation, larger particles formed in the bulk deposited on and between the scaling islands, slightly hindering water transport but increasing electrical conductivity in the fouling layer due to cake enhanced concentration polarization of ions.

For Ca-P (Fig. 8b), the results imply that mineral fouling is initiated by bulk precipitation, occurring at very low supersaturation with almost no induction time. At the conditions studied, the precipitant is initially composed of amorphous, highly hydrated sub-micron particles, which deposit on the membrane. Consequently, a porous fouling layer is formed, hindering water transport but allowing ions to pass through. With the increase in supersaturation and at longer filtration time, the smaller particles aggregated, followed by dehydration and consolidation of the amorphous



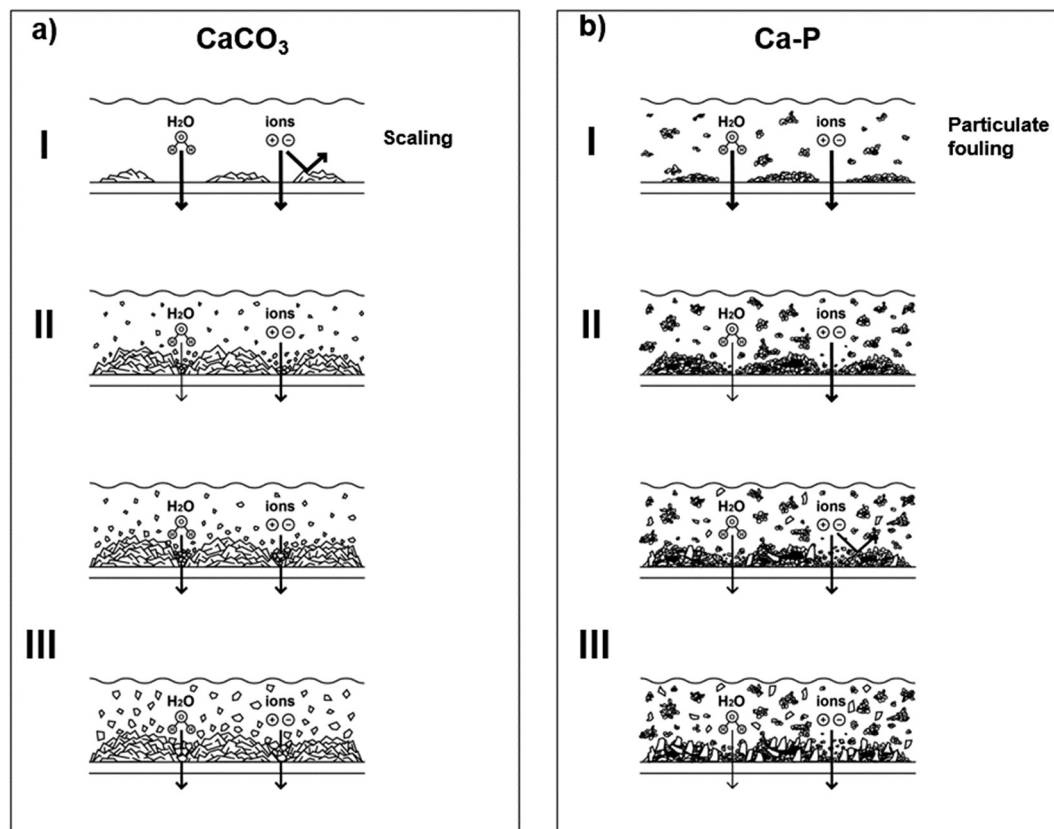


**Fig. 8** Illustration of the proposed mechanism of mineral fouling evolution with time, based on the real-time monitoring and post-filtration microscopy (a) CaCO<sub>3</sub> scaling evolution stages initiated with scaling/surface crystallization and transforms to particulate fouling; (b) Ca-P fouling evolution stages, initially with amorphous particulates and transforms into crystalline particulates.

Ca-P, as part of its ageing process (Oswald's rule). Some of the aggregates may have detached from the surface by shear force. This resulted in a dense layer with holes and cracks, allowing faster ion passage but hindering water transport. After a further increase in supersaturation and filtration time, the phase transition progresses, and plate-shaped crystals appear. These crystals deposit and accumulate on the membrane, forming a top cake layer that inhibits water transport, but increased electrical conductivity through cake enhanced concentration polarization of ions.

Our findings have practical implications for the control and mitigation of mineral fouling, which is essential for obtaining a high recovery in wastewater effluent nanofiltration and reverse osmosis. We show evidence that under typical effluent filtration conditions, ACP formed in the retentate solution controls the initial stages of Ca-P fouling. Therefore, modifying the membrane surface is not expected to contribute to scaling mitigation significantly. We also observed that ACP starts precipitating at a very low supersaturation level and with practically no induction time, making the saturation index a practical scaling control parameter. In contrast, CaCO<sub>3</sub> fouling is initially controlled by surface scaling, which starts after a significantly shorter induction time compared to bulk precipitation. Compared to CaCO<sub>3</sub> scaling, Ca-P fouling is more reversible and could be

more easily controlled by crossflow cleaning or backwash. Acid cleaning should also be more effective for a porous layer (as compared to the crystalline scaling layer) since the liquid–solid contact area is higher. Thus, CaCO<sub>3</sub> scaling should be avoided, whereas some extent of Ca-P fouling can be tolerated and removed. We found that when the retained solution contains larger and more crystalline mineral particles, the effect of fouling on filtration performance is less severe. This raises interesting possibilities to control mineral fouling by introducing seeds at an intermediate filtration stage. In our future work, we plan to implement and test this novel strategy.

## Conflicts of interest

There are no conflicts of interest to declare.

## Acknowledgements

This work was funded by the Ministry of Science and Technology (MOST) Israel, under the framework of German-Israeli Water Technology Research (Project: 8764961). We also thank the Young Scientists Exchange Program (YSEP) of the BMBF-MOST Cooperation in Water Technology Research.

## References

- 1 G. Oron, L. Gillerman, N. Buriakovsky, A. Bick, M. Gargir and Y. Dolan, *et al.*, Membrane technology for advanced wastewater reclamation for sustainable agriculture production, *Desalination*, 2008, **218**(1–3), 170–180, Available from: <https://www.sciencedirect.com/science/article/pii/S001191640700522X>.
- 2 S. A. A. N. Almuktar, S. N. Abed and M. Scholz, Wetlands for wastewater treatment and subsequent recycling of treated effluent: a review, *Environ. Sci. Pollut. Res.*, 2018, **25**(24), 23595–23623.
- 3 M. Farhadkhani, M. Nikaeen, G. Yadegarfar, M. Hatamzadeh, H. Pourmohammadbagher and Z. Sahbaei, *et al.*, Effects of irrigation with secondary treated wastewater on physicochemical and microbial properties of soil and produce safety in a semi-arid area, *Water Res.*, 2018, **144**, 356–364.
- 4 E. Friedler, Water reuse - An integral part of water resources management: Israel as a case study, *Water Policy*, 2001, **3**(1), 29–39.
- 5 Q. K. Tran, K. A. Schwabe and D. Jassby, Wastewater reuse for agriculture: Development of a regional water reuse decision-support model (RWRM) for cost-effective irrigation sources, *Environ. Sci. Technol.*, 2016, **50**(17), 9390–9399.
- 6 T. Wintgens, T. Melin, A. Schäfer, S. Khan, M. Muston and D. Bixio, *et al.*, The role of membrane processes in municipal wastewater reclamation and reuse, *Desalination*, 2005, **178**(1–3 SPEC. ISS.), 1–11.
- 7 X. Garcia and D. Pargament, Reusing wastewater to cope with water scarcity: Economic, social and environmental considerations for decision-making, *Resour., Conserv. Recycl.*, 2015, **101**, 154–166.
- 8 S. Murgolo, S. Franz, H. Arab, M. Bestetti, E. Falletta and G. Mascolo, Degradation of emerging organic pollutants in wastewater effluents by electrochemical photocatalysis on nanostructured TiO<sub>2</sub> meshes, *Water Res.*, 2019, **164**, 114920.
- 9 C. Grandclément, I. Seyssiecq, A. Piram, P. Wong-Wah-Chung, G. Vanot and N. Tiliacos, *et al.*, From the conventional biological wastewater treatment to hybrid processes, the evaluation of organic micropollutant removal: A review, *Water Res.*, 2017, **111**, 297–317, Available from: <https://www.sciencedirect.com/science/article/pii/S0043135417300052>.
- 10 Y. Luo, W. Guo, H. Hao, L. Duc, F. Ibney and J. Zhang, *et al.*, A review on the occurrence of micropollutants in the aquatic environment and their fate and removal during wastewater treatment, *Sci. Total Environ.*, 2014, **473–474**, 619–641, DOI: [10.1016/j.scitotenv.2013.12.065](https://doi.org/10.1016/j.scitotenv.2013.12.065).
- 11 L. D. Nghiem and T. Fujioka, Removal of Emerging Contaminants for Water Reuse by Membrane Technology, in *Emerging Membrane Technology for Sustainable Water Treatment*, 2016.
- 12 S. Bunani, E. Yörükoğlu, G. Sert, Ü. Yüksel, M. Yüksel and N. Kabay, Application of nanofiltration for reuse of municipal wastewater and quality analysis of product water, *Desalination*, 2013, **315**, 33–36, Available from: <https://www.sciencedirect.com/science/article/pii/S0011916412006108>.
- 13 A. W. Mohammad, Y. H. Teow, W. L. Ang, Y. T. Chung, D. L. Oatley-Radcliffe and N. Hilal, Nanofiltration membranes review: Recent advances and future prospects, *Desalination*, 2015, **356**, 226–254, Available from: <https://www.sciencedirect.com/science/article/pii/S0011916414005773#bb0795>.
- 14 S. Lee and C.-H. Lee, Scale formation in NF/RO: Mechanism and control, *Water Sci. Technol.*, 2005, **51**, 267–275.
- 15 A. I. Schäfer, A. G. Fane and T. D. Waite, Nanofiltration of natural organic matter: Removal, fouling and the influence of multivalent ions, *Desalination*, 1998, **118**(1–3), 109–122, Available from: <https://www.sciencedirect.com/science/article/pii/S0011916498001040>.
- 16 O. Nir, R. Sengpiel and M. Wessling, Closing the cycle: Phosphorus removal and recovery from diluted effluents using acid resistive membranes, *Chem. Eng. J.*, 2018, **346**, 640–648.
- 17 N. Voutchkov, Overview of seawater concentrate disposal alternatives, *Desalination*, 2011, **273**(1), 205–219, Available from: <https://www.sciencedirect.com/science/article/pii/S0011916410007332>.
- 18 I. S. Chang, S. S. Lee and E. K. Choe, Digital textile printing (DTP) wastewater treatment using ozone and membrane filtration, *Desalination*, 2009, **235**(1–3), 110–121.
- 19 C. Kappel, A. J. B. Kemperman, H. Temmink, A. Zwijnenburg, H. H. M. Rijnaarts and K. Nijmeijer, Impacts of NF concentrate recirculation on membrane performance in an integrated MBR and NF membrane process for wastewater treatment, *J. Membr. Sci.*, 2014, **453**, 359–368.
- 20 L. F. Greenlee, F. Testa, D. F. Lawler, B. D. Freeman and P. Moulin, The effect of antiscalant addition on calcium carbonate precipitation for a simplified synthetic brackish water reverse osmosis concentrate, *Water Res.*, 2010, **44**(9), 2957–2969.
- 21 G. Greenberg, D. Hasson and R. Semiat, Limits of RO recovery imposed by calcium phosphate precipitation, *Desalination*, 2005, **183**(1–3), 273–288.
- 22 T. Tong, A. F. Wallace, S. Zhao and Z. Wang, Mineral scaling in membrane desalination: Mechanisms, mitigation strategies, and feasibility of scaling-resistant membranes, *J. Membr. Sci.*, 2019, **579**, 52–69.
- 23 M. Chaussemier, E. Pourmohtasham, D. Gelus, N. Pécou, H. Perrot and J. Lédion, *et al.*, State of art of natural inhibitors of calcium carbonate scaling. A review article, *Desalination*, 2015, **356**, 47–55.
- 24 Z. Steiner, H. Rapaport, Y. Oren and R. Kasher, Effect of surface-exposed chemical groups on calcium-phosphate mineralization in water-treatment systems, *Environ. Sci. Technol.*, 2010, **44**(20), 7937–7943.
- 25 A. Antony, J. How, S. Gray, A. E. Childress, P. Le-clech and G. Leslie, Scale formation and control in high pressure membrane water treatment systems : A review, *J. Membr. Sci.*, 2011, **383**(1–2), 1–16, DOI: [10.1016/j.memsci.2011.08.054](https://doi.org/10.1016/j.memsci.2011.08.054).
- 26 M. N. Mangal, S. G. Salinas-Rodriguez, J. Dusseldorp, A. J. B. Kemperman, J. C. Schippers and M. D. Kennedy, *et al.*,

- Effectiveness of antiscalants in preventing calcium phosphate scaling in reverse osmosis applications, *J. Membr. Sci.*, 2021, **623**, 119090.
- 27 C. A. C. Van De Lisdonk, J. A. M. Van Paassen and J. C. Schippers, Monitoring scaling in nanofiltration and reverse osmosis membrane systems, *Desalination*, 2000, **132**(1–3), 101–108.
  - 28 S. Lee and C. H. Lee, Effect of operating conditions on CaSO<sub>4</sub> scale formation mechanism in nanofiltration for water softening, *Water Res.*, 2000, **34**(15), 3854–3866.
  - 29 P. G. Klepetsanis and P. G. Koutsoukos, Precipitation of calcium sulfate dihydrate at constant calcium activity, *J. Cryst. Growth*, 1989, **98**(3), 480–486.
  - 30 T. Chen, A. Neville and M. Yuan, Influence of Mg<sup>2+</sup> on CaCO<sub>3</sub> formation-bulk precipitation and surface deposition, *Chem. Eng. Sci.*, 2006, **61**(16), 5318–5327.
  - 31 H. Roques and A. Girou, Kinetics of the formation conditions of carbonate tartars, *Water Res.*, 1974, **8**(11), 907–920.
  - 32 K. Rathinam, Y. Oren, W. Petry, D. Schwahn and R. Kasher, Calcium phosphate scaling during wastewater desalination on oligoamide surfaces mimicking reverse osmosis and nanofiltration membranes, *Water Res.*, 2018, **128**, 217–225.
  - 33 M. Kaganovich, W. Zhang, V. Freger and R. Bernstein, Effect of the membrane exclusion mechanism on phosphate scaling during synthetic effluent desalination, *Water Res.*, 2019, **161**, 381–391.
  - 34 J. Gilron and D. Hasson, Calcium sulphate fouling of reverse osmosis membranes: Flux decline mechanism, *Chem. Eng. Sci.*, 1987, **42**(10), 2351–2360.
  - 35 J. Y. Choi, T. Lee, Y. Cheng and Y. Cohen, Observed Crystallization Induction Time in Seeded Gypsum Crystallization, *Ind. Eng. Chem. Res.*, 2019, **58**(51), 23359–23365, DOI: [10.1021/acs.iecr.9b06050](https://doi.org/10.1021/acs.iecr.9b06050).
  - 36 C. Tzotzi, T. Pahiadaki, S. G. Yiantsios, A. J. Karabelas and N. Andritsos, A study of CaCO<sub>3</sub> scale formation and inhibition in RO and NF membrane processes, *J. Membr. Sci.*, 2007, **296**(1–2), 171–184.
  - 37 P. Xu, C. Bellona and J. E. Drewes, Fouling of nanofiltration and reverse osmosis membranes during municipal wastewater reclamation: Membrane autopsy results from pilot-scale investigations, *J. Membr. Sci.*, 2010, **353**(1–2), 111–121.
  - 38 J. de Grooth, B. Haakmeester, C. Wever, J. Potreck, W. M. de Vos and K. Nijmeijer, Long term physical and chemical stability of polyelectrolyte multilayer membranes, *J. Membr. Sci.*, 2015, **489**, 153–159, Available from: <https://www.sciencedirect.com/science/article/pii/S0376738815003622>.
  - 39 D. Gregurec, M. Olszyna, N. Politakos, L. Yate, L. Dahne and S. E. Moya, Stability of polyelectrolyte multilayers in oxidizing media: a critical issue for the development of multilayer based membranes for nanofiltration, *Colloid Polym. Sci.*, 2015, **293**(2), 381–388, DOI: [10.1007/s00396-014-3423-5](https://doi.org/10.1007/s00396-014-3423-5).
  - 40 D. Menne, J. Kamp, J. Erik Wong and M. Wessling, Precise tuning of salt retention of backwashable polyelectrolyte multilayer hollow fiber nanofiltration membranes, *J. Membr. Sci.*, 2016, **499**, 396–405, DOI: [10.1016/j.memsci.2015.10.058](https://doi.org/10.1016/j.memsci.2015.10.058).
  - 41 O. Oren, I. Gavrieli, A. Burg, J. Guttman and B. Lazar, Manganese mobilization and enrichment during soil aquifer treatment (SAT) of effluents, the Dan Region Sewage Reclamation Project (Shafdan), Israel, *Environ. Sci. Technol.*, 2007, **41**(3), 766–772.
  - 42 S. Bannwarth, T. Trieu, C. Oberschelp and M. Wessling, On-line monitoring of cake layer structure during fouling on porous membranes by in situ electrical impedance analysis, *J. Membr. Sci.*, 2016, **503**, 188–198.
  - 43 O. Nir, T. Trieu, S. Bannwarth and M. Wessling, Microfiltration of deformable microgels, *Soft Matter*, 2016, **12**(31), 6512–6517.
  - 44 A. Antony, T. Chilcott, H. Coster and G. Leslie, In situ structural and functional characterization of reverse osmosis membranes using electrical impedance spectroscopy, *J. Membr. Sci.*, 2013, **425–426**, 89–97.
  - 45 K. Chellappah, S. Tarleton and R. Wakeman, The porosity, permeability and restructuring of heterogeneous filter cakes, *Chem. Eng. Technol.*, 2010, **33**(8), 1283–1289.
  - 46 N. Andritsos, A. J. Karabelas and P. G. Koutsoukos, Morphology and structure of CaCO<sub>3</sub> scale layers formed under isothermal flow conditions, *Langmuir*, 1997, **13**(10), 2873–2879.
  - 47 A. T. K. Tran, Y. Zhang, D. De Corte, J. Hannes, W. Ye and P. Mondal, *et al.*, P-recovery as calcium phosphate from wastewater using an integrated electrodialysis/crystallization process, *J. Cleaner Prod.*, 2014, **77**, 140–151.
  - 48 E. H. Kim, Y. S. Bin, H. C. Jung and E. J. Lee, Hydroxyapatite crystallization from a highly concentrated phosphate solution using powdered converter slag as a seed material, *J. Hazard. Mater.*, 2006, **136**(3), 690–697.
  - 49 B. Xie, T. J. Halter, B. M. Borah and G. H. Nancollas, Tracking amorphous precursor formation and transformation during induction stages of nucleation, *Cryst. Growth Des.*, 2014, **14**(4), 1659–1665.
  - 50 V. Čadež, I. Erceg, A. Selmani, D. Domazet Jurašin, S. Šegota and D. Lyons, *et al.*, Amorphous Calcium Phosphate Formation and Aggregation Process Revealed by Light Scattering Techniques, *Crystals*, 2018, **8**(6), 254, Available from: <https://www.mdpi.com/2073-4352/8/6/254>.